

Angular Resolution of a Bayesian Search for Anisotropic Stochastic Gravitational Wave Backgrounds with LISA

Malachy Bloom ^{1,*}, Alexander W. Criswell ^{2,3,4,5} and Vuk Mandic ^{2,3}

¹*Carleton College, Northfield, MN 55057, USA*

²*Minnesota Institute for Astrophysics, University of Minnesota, Minneapolis, MN 55455, USA*

³*School of Physics and Astronomy, University of Minnesota, Minneapolis, MN 55455, USA*

⁴*Department of Physics and Astronomy, Vanderbilt University, Nashville, TN 37240*

⁵*Department of Life and Physical Sciences, Fisk University, Nashville, TN 37208*

(Dated: December 24, 2024)

The Laser Interferometer Space Antenna (LISA), a spaceborne gravitational wave (GW) detector set to launch in 2035, will observe several stochastic GW backgrounds in the mHz frequency band. At least one of these signals — arising from the tens of millions of unresolved white dwarf binaries in the Milky Way — is expected to be highly anisotropic on the sky. We evaluate the angular resolution of LISA and its ability to characterize anisotropic stochastic GW backgrounds (ASGWBs) using the Bayesian Spherical Harmonic formalism in the Bayesian LISA Inference Package (BLIP). We use BLIP to simulate and analyze ASGWB signals in LISA across a large grid in total observing time, ASGWB amplitude, and angular size. We consider the ability of the BLIP anisotropic search algorithm to both characterize single point sources and to separate two point sources on the sky, using a full-width half-max (FWHM) metric to measure the quality and spread of the recovered spatial distributions. We find that the number of spherical harmonic coefficients used in the anisotropic search model is the primary factor that limits the search’s angular resolution. Notably, this trend continues until computational limitations become relevant around $\ell_{\max} = 16$; this exceeds the maximum angular resolution achieved by other map-making techniques for LISA ASGWBs.

I. INTRODUCTION

A. Anisotropic Stochastic Gravitational Wave Backgrounds in LISA

The Laser Interferometer Space Antenna (LISA) is a future spaceborne mHz-band gravitational-wave (GW) observatory set to launch in 2035 [1]. A wide variety of astrophysical sources are expected to emit GWs in the LISA band (see Amaro-Seoane *et al.* [2] for a review); while some of these signals are expected to be individually detectable, many others will remain unresolved, instead contributing to one of several stochastic gravitational wave backgrounds (SGWBs). SGWBs are confusion noise formed by the superposition of many unresolved astrophysical or cosmological GW sources. Recently, Agazie *et al.* [3] reported evidence for such a signal in the nHz band using pulsar timing arrays. LISA data is expected to feature a number of mHz SGWBs, including those from galactic (and extragalactic) white dwarf binary systems [4–6], extreme-mass-ratio inspirals [7], and stellar-origin compact binaries (e.g., [8]), among others. Notably, the SGWB from unresolved galactic white dwarf binaries in the Milky Way is expected to be so loud as to sit above the LISA noise curve, and is therefore termed the “galactic foreground” [4, 5]. Both the galactic foreground and potential SGWBs from white dwarf binaries in satellite galaxies of the Milky Way [6] will be highly anisotropic due to the spatial distribution of their compo-

nent sources. Additionally, it is possible LISA may contain SGWBs from a number of cosmological sources, such as inflation, phase transitions, cosmic (super)strings, and primordial black holes; see Caprini and Figueroa [9] for a review. All SGWBs from non-local sources, astrophysical and cosmological alike, can be expected to contain some level of anisotropy due to the large scale structure of the universe, deriving from both the specific source distribution and propagation effects [10–15]. Characterizing the spatial distribution on the sky of anisotropic SGWBs (ASGWBs) is crucial; not only does proper subtraction of an ASGWB require accurate description of its spatial distribution, but accurate spatial characterization could also enable scientific gains from the ASGWBs in question[e.g., 16]. Moreover, constraining the level of anisotropy of astrophysical SGWBs can inform our understanding of the large-scale structure of the Universe [17, 18]. Finally, constraining the anisotropy of potential cosmological SGWBs could provide a novel window into the physics of the early Universe [19].

B. Anisotropic SGWB Searches

Several analyses exist to search for and characterize ASGWBs in ground-based GW detectors [20, 21] and Pulsar Timing Arrays [22–27]. For LISA, there are several studies that use Fisher-matrix or other frequentist approaches [19, 28–33]. Additionally, Bayesian methods have been developed for LISA analyses of the anisotropic Galactic foreground and other local-universe ASGWBs [34–37]. However, the only extant analysis infrastructure capable of performing a generic Bayesian anisotropic

* bloomm@carleton.edu

search for SGWBs in LISA is, to the authors' knowledge at time of writing, the Bayesian LISA Inference Package (BLIP). BLIP is an open source Python package capable of end-to-end simulation and Bayesian inference of isotropic and anisotropic SGWBs in LISA, first presented in Banagiri *et al.* [38].¹ A full description of BLIP and its spherical harmonic ASGWB search can be found in Banagiri *et al.* [38]; details relevant to this study are presented in brief in §II A.

Given the potential scientific gains that accompany accurate characterization of ASGWBs in LISA, it is important to understand the capabilities of LISA for characterizing anisotropic sources. LISA's angular resolution has been previously considered: first by Peterseim *et al.* [39], Cutler [40], Moore and Hellings [41] and followed thereafter with studies of angular resolution to ASGWBs for frequentist approaches specifically [19, 42–45]. While earlier studies [42, 43] found that LISA's angular resolution would be limited to $\ell_{\max} \leq 4$, the improved formalism of Contaldi *et al.* [44] may be able to achieve a limit of $\ell_{\max} \lesssim 15$ for the optimal case ($\ell_{\max} \lesssim 8$ for more realistic considerations [19, 45]). However, the angular resolution of Bayesian ASGWB searches with LISA has not previously been considered. Doing so is especially important given that LISA ASGWB searches are likely to take place in a global fit setting [e.g., 46, 47] and as such will necessarily be Bayesian in nature.

We therefore investigate the angular resolution of LISA and its ability to characterize ASGWBs with a Bayesian approach using the Bayesian spherical harmonic search in BLIP. We consider the ability of the spherical harmonic Bayesian search to characterize both single and double point-source ASGWBs across a broad range of signal amplitudes, spot sizes, and choice of spherical harmonic ℓ_{\max} used to parameterize the analysis. We discuss the BLIP Bayesian spherical harmonic search in §II A; the ASGWB simulation method is outlined in §II B. Analyses of single-point and two-point source configurations are presented in §III A and §III B, respectively. Discussion of these results and their implications for LISA's angular resolution with Bayesian ASGWB searches is given in §IV, alongside directions of future inquiry.

II. METHODOLOGY

A. The BLIP Anisotropic Analysis

BLIP's Bayesian spherical harmonic ASGWB search performs simultaneous inference of the LISA noise spectrum, the ASGWB spectrum, and the ASGWB's spatial distribution as represented in a spherical harmonic expansion. The underlying mechanics of the BLIP ASGWB search algorithm are based on formalisms developed in Cornish and Larson [48] and Cornish [49], with

the central addition of the spherical harmonic treatment described below and discussed in detail in Banagiri *et al.* [38]. Importantly, the BLIP anisotropic search explicitly models the motion of the LISA detector through space and, accordingly, the time-dependence of its directional response to ASGWBs. A full derivation of this response in the spherical harmonic basis can be found in Banagiri *et al.* [38]. We use *dynesty* [50] nested sampling to produce Bayesian posterior distributions on all model parameters. The LISA instrumental noise is modelled with the two-component position and acceleration noise model given in the LISA proposal [1]:

$$\begin{aligned} S_p(f) &= N_p \left[1 + \left(\frac{2 \text{ mHz}}{f} \right)^4 \right] \text{ Hz}^{-1}, \\ S_a(f) &= \left[1 + \left(\frac{0.4 \text{ mHz}}{f} \right)^2 \right] \\ &\quad \times \left[1 + \left(\frac{f}{8 \text{ mHz}} \right)^4 \right] \times \frac{N_a}{(2\pi f)^4} \text{ Hz}^{-1}, \end{aligned} \quad (1)$$

where N_a and N_p are independent parameters to be inferred. We assume the spectral and spatial dependence of the ASGWB can be separated; that is we model the ASGWB as

$$\Omega_{\text{GW}}(f, \mathbf{n}; \vec{\theta}) = \Omega(f; \vec{\theta}) \mathcal{P}(\mathbf{n}), \quad (2)$$

where $\Omega(f; \vec{\theta})$ is the spectral shape of the SGWB parameterized by $\vec{\theta}$, given in terms of the dimensionless GW energy density², and $\mathcal{P}(\mathbf{n})$ is the corresponding spatial distribution (whose integral over the sky is normalized to 1). For this study, we assume a power law spectral shape for the ASGWB:

$$\Omega(f; \vec{\theta}) = \Omega_{\text{ref}} \left(\frac{f}{f_{\text{ref}}} \right)^\alpha, \quad (3)$$

where $\vec{\theta} = \{\Omega_{\text{ref}}, \alpha\}$, Ω_{ref} is the dimensionless GW energy density evaluated at the reference frequency $f_{\text{ref}} = 25 \text{ Hz}$, and α is the power law spectral index.

The ASGWB spatial distribution $\mathcal{P}(\mathbf{n})$ is modelled using a spherical harmonic expansion up to a user-defined value of ℓ_{\max} . Specifically, BLIP infers the spherical harmonic expansion coefficients $b_{\ell m}$ of the *square root* of the power on the sky, $\mathcal{S}(\mathbf{n})$, such that

$$\begin{aligned} \mathcal{S}(\mathbf{n}) &= \sqrt{\mathcal{P}(\mathbf{n})} = \left[\sum_{\ell=0}^{\ell_{\max}^a} \sum_{m=-\ell}^{\ell} a_{\ell m} Y_{\ell m}(\mathbf{n}) \right]^{1/2} \\ &= \sum_{\ell=0}^{\ell_{\max}^b} \sum_{m=-\ell}^{\ell} b_{\ell m} Y_{\ell m}(\mathbf{n}). \end{aligned} \quad (4)$$

² This is related to the strain power spectrum of the ASGWB, S_{GW} , by $\Omega(f) = (2\pi^2 f^3 / 3H_0^2) S_{\text{GW}}(f)$. We assume a value of $H_0 = 67.88 \text{ km/s/Mpc}$.

¹ <https://github.com/sharanbng/blip>

Fitting the square root of the distribution mathematically ensures that all possible inferred distributions of power on the sky are not only real but also non-negative (a non-trivial problem; see Banagiri *et al.* [38]). The $b_{\ell m}$ s are related to the usual spherical harmonic $a_{\ell m}$ s via a Clebsch-Gordan decomposition:

$$a_{\ell m} = \sum_{L,M} \sum_{L',M'} b_{LM} b_{L'M'} \sqrt{\frac{(2L+1)(2L'+1)}{4\pi(2L+1)}} \times C_{\ell m}^{LM,L'M'} C_{\ell 0}^{L0,L'0}, \quad (5)$$

with associated selection rules [38]. An important consequence of this is that the truncation ℓ_{\max} for each expansion are related by $\ell_{\max}^a = 2\ell_{\max}^b$.

Each analysis therefore infers the log power law amplitude $\log_{10} \Omega_{\text{ref}}$, the power law index α , and the spherical harmonic coefficients $b_{\ell m}$. These latter are parameterized in terms of their amplitude $|b_{\ell m}|$ (for all ℓ, m) and their phase $\phi_{\ell m}$ (for complex $b_{\ell m}$ coefficients, i.e. those with $m \neq 0$). The priors used in this work are as follows:

- $\pi(\log_{10} \Omega_{\text{ref}}) = \mathcal{U}(-14, 8)$
- $\pi(\alpha) = \mathcal{U}(-5, 5)$
- $\pi(b_{\ell 0}) = \mathcal{U}(-3, 3)$ for real $b_{\ell 0}$
- $\pi(|b_{\ell m}|) = \mathcal{U}(0, 3)$ for complex $b_{\ell m}$, $m \neq 0$
- $\pi(\phi_{\ell m}) = \mathcal{U}(-\pi, \pi)$ for complex $b_{\ell m}$, $m \neq 0$

For further details on the BLIP anisotropic treatment, its Fourier-domain likelihood, and the underlying mechanics of the BLIP analysis infrastructure, refer to Banagiri *et al.* [38].

B. ASGWB Simulations

We consider two types of simulated ASGWB: one consisting of a single, localized source (“single point” simulations), and one consisting of two such sources (“two point” simulations). Each simulated ASGWB has a power-law spectrum with spectral index $\alpha = 2/3$ and has its spatial distribution represented in the spherical harmonic basis for direct comparison to the BLIP ASGWB analysis. For the single-point case, we perform simulations of LISA ASGWB data across a grid in three major parameters: $\ell_{\max, \text{inj}}^a$, the spherical harmonic cutoff used to simulate the ASGWB in the spherical harmonic basis; Ω_{ref} , the amplitude of the simulated power-law ASGWB spectrum; and T_{obs} , the duration of the simulated data. For the two-point case, we additionally vary $\Delta\phi$, the angular separation (in radians) between the two component sources. All single-point sources are simulated at an ecliptic sky position of $(\theta, \phi) = (\frac{\pi}{2}, \frac{\pi}{2})$. The sky positions for the two-point case vary due to changing their separation $\Delta\phi$; the sky positions $(\theta_1, \phi_1), (\theta_2, \phi_2)$ for all two-point simulations are given in Table III. We do not

otherwise vary sky location as a parameter of interest as the directional sensitivity of LISA is known and can be accounted for analytically.

We analyze each simulation at several different values of ℓ_{\max}^a , the spherical harmonic ℓ_{\max} in the recovery model.³ All simulations and analyses in this work use skymaps with a Healpy [51] `nside` (pixel map resolution) of 32 (corresponding angular scale of $\ell_a \approx 98$), and simulate/analyze data in the X – Y – Z time-delay interferometry channels [52]. A summary of the simulation grid can be found in Table I; a full list of all simulations and associated parameters can be found in Appendix B. The maximum values of ℓ_{\max}^a and $\ell_{\max, \text{inj}}^a$ are driven by computational limitations due to both the memory requirements and convolution cost of the $3 \times 3 \times n_f \times n_t \times n_n \times \ell_{\max}^b (\ell_{\max}^b + 1)$ LISA spherical harmonic response, where n_f , n_t , and n_n are the number of frequency bins, time segments, and sky pixels,⁴ respectively.⁵ The maximum of Ω_{ref} is chosen to be comparable to the amplitude of the Galactic white dwarf binary foreground. We simulated and analyzed ASGWBs with values of Ω_{ref} below the listed minimum, but were unable to obtain consistent recoveries with the observing durations considered due to the simulated signals’ low signal-to-noise ratio (SNR); see §III A. We therefore did not fill out the full grid at these subthreshold values of Ω_{ref} to avoid undue waste of computational resources. It will be important in future to explore the realistic case of using a Bayesian spherical harmonic search to characterize low-SNR ASGWBs in the presence of the Galactic foreground over the nominal LISA mission duration. However, as this study is concerned with the general performance and limitations of Bayesian LISA ASGWB analyses, we leave a dedicated study of this more realistic case to future work (and note that a proof-of-concept of such a search can be found in Rieck *et al.* [6]). The range of T_{obs} is chosen so as to probe the effects of LISA’s orbit on the angular resolution of our anisotropic search. While the nominal LISA mission duration is 4 years, the scaling of SGWB sensitivity with observing time is well-understood [53] and further complete orbits are expected to follow the standard $\sqrt{T_{\text{obs}}}$. Finally, the range of $\Delta\phi$ spans $(\pi/5, \pi)$ radians at an angular step of $\pi/5$, chosen to maintain feasibility in total number of simulations performed while still exploring the full gamut of two-point

³ Note that ℓ_{\max}^a and $\ell_{\max, \text{inj}}^a$ need not be the same; we in fact consider the effects of mismatch between these parameters in §III A. We restrict analysis-simulation pairs such that $\ell_{\max}^a \leq \ell_{\max, \text{inj}}^a$.

⁴ Note that the final response used at sample-time is integrated over sky direction, so the convolutional cost at sample time is “only” driven by matrix operations with a $3 \times 3 \times n_f \times n_t \times \ell_{\max}^b (\ell_{\max}^b + 1)$ array.

⁵ “Computational limits” can be taken to mean either exceeding ~ 2 TB of RAM or having such a high likelihood evaluation cost that the `dynesty` sampler used in this work would not converge on a timescale of $\lesssim 1$ month (wall time).

Parameter	Minimum	Maximum
ℓ_{\max}^a	4	16
Ω_{ref}	1.6×10^{-9}	4.0×10^{-7}
T_{obs}	3 months	1 year
$\ell_{\max, \text{inj}}^a$	4	16
$\Delta\phi$	$\pi/5$	π

TABLE I. Summary of simulation parameters.

separations on the sky.

C. Angular Resolution Metrics

We employ two metrics based on the full-width-half-maximum (FWHM) measure to quantitatively evaluate BLIP’s recovery of the simulated ASGWB spatial distributions for the single point and two point cases, respectively. To calculate the FWHM of a point source recovery described by a given posterior sample, we compute the Healpy skymap corresponding to its $b_{\ell m s}$, locating the maximum energy-density pixel within that skymap, and iteratively combining adjacent pixels with energy-density greater than half of the peak value until no such pixels remain. This process creates a contour around the peak; an example of these contours can be seen in Fig. 1. For the single point case, we then compute the fraction of the sky that lies within the contour, yielding a metric — hereafter the “SP metric” — that corresponds to the spot size; the SP metric value is therefore inversely proportional to the angular resolution of the search. This metric is computed for every posterior sample of a given single-point BLIP analysis; the data points and error bars shown in Figs. 2 and 3 are the means and 95% credible intervals of the resulting distribution for each analysis.

For the two point case, we compute the ratio of the (minimum) angular separation between the FWHM contours of each source separately and the combined FWHM fraction of the sky, following a similar approach to that of [20]. The two-point metric (TP metric) therefore quantifies the angular resolution by the ratio of separation to the total spot size; a larger value of the TP metric corresponds to better angular resolution. If two distinct FWHM contours cannot be found for a given skymap, the separation is taken to be zero (i.e., the sources are not resolved from one another) and the TP metric is therefore equal to zero. Examples of the TP metric contours for several different intrinsic angular separations are shown in Fig. 4. As for the SP metric, this calculation is performed for every posterior sample and the TP metric values and error bars shown in Figs. 5 and 6 are the means and 95% credible intervals of the resulting distributions.

For each metric, we consider an approximate heuristic for comparison’s sake. The approximate angular scale that can be probed by a spherical harmonic parameteri-

zation with a given ℓ_{\max}^a is

$$\theta \sim \frac{\pi}{\ell_{\max}^a}. \quad (6)$$

The approximate limit of the SP metric, assuming a 2D Gaussian point source with angular standard deviation $\frac{\theta}{2}$, will then be

$$\text{SP}_{\min} = \sin^2 \left(\frac{1.1809}{4} \frac{\pi}{\ell_{\max}^a} \right), \quad (7)$$

i.e., the fractional solid angle subtended by the FWHM of the Gaussian at an angular radius of $\theta_{\text{FWHM}} \simeq 1.1809 \frac{\theta}{2}$. The equivalent heuristic for the TP metric for a given simulated angular separation $\Delta\phi$ will then be the ratio of their angular separation, less $2 \times \theta_{\text{FWHM}}$, to the combined area of each point source recovery (i.e., the sum of the SP metric of each source):

$$\text{TP}_{\max} = \frac{\max \left(\Delta\phi - 1.1809 \frac{\pi}{\ell_{\max}^a}, 0 \right)}{2 \text{SP}_{\min}}. \quad (8)$$

The resulting heuristic curves for $\text{SP}_{\min}(\ell_{\max}^a)$ and $\text{TP}_{\max}(\Delta\phi)|_{\ell_{\max}^a=8}$ are shown for comparison to our results in Figs. 2 and 6, respectively. We stress that these are necessarily approximate measures, and serve primarily to contextualize the trends seen in the data.

III. RESULTS

We present Bayesian spherical harmonic analyses and their associated SP/TP metrics for all single-point and two-point simulations as described in Tables II and III, respectively. Each simulation is analyzed with BLIP as described in §II A. For visualization purposes, all skymaps shown are evaluated for $\Omega(f = 1\text{mHz})$. All data points and error bars are means and 95% credible intervals of their respective metric.

A. Single Point Source

1. Dependence on ℓ_{\max}^a

To investigate angular resolution dependence on the choice of ℓ_{\max}^a used in the analysis, we analyze single-point sources with 4 different values of Ω_{ref} and vary ℓ_{\max}^a from 4 to 16. Figure 2 shows the associated SP metric for each analysis. As ℓ_{\max}^a increases the angular resolution improves drastically, whereas there is no obvious dependence on the ASGWB amplitude Ω_{ref} apart from improving the error bars. The overall trend follows that of the approximate limit’s dependence on ℓ_{\max}^a , albeit at a slight positive offset in the value of the SP metric.

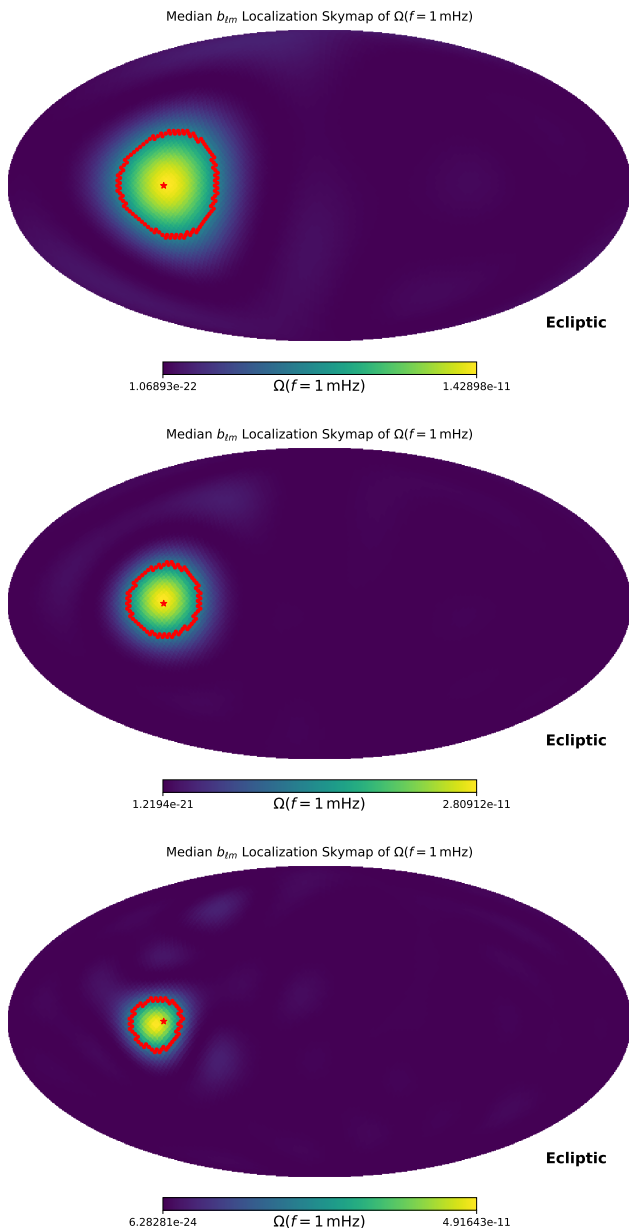


FIG. 1. Posterior median ASGWB energy density skymaps with FWHM contours shown in red and the true (simulated) location of the point source indicated with a red star. These plots were produced via the analyses discussed in §II B-II C for simulated ASGWBs with $\Omega_{\text{ref}} = 8 \times 10^{-9}$, $T_{\text{obs}} = 3$ months, and (from top to bottom) $\ell_{\text{max}}^a = 6, 10, 16$. As ℓ_{max}^a increases, the ability of the Bayesian ASGWB analysis to resolve the point source increases.

2. Dependence on ASGWB Amplitude/Observing Time

The dependence on Ω_{ref} and T_{obs} is more closely inspected in Fig. 3. We vary Ω_{ref} from 1.6×10^{-9} to 4×10^{-7} for total observing time, T_{obs} , ranging from 3 months to 1 year. No significant dependence of the SP metric on Ω_{ref} or T_{obs} is apparent for recovered sources. However,

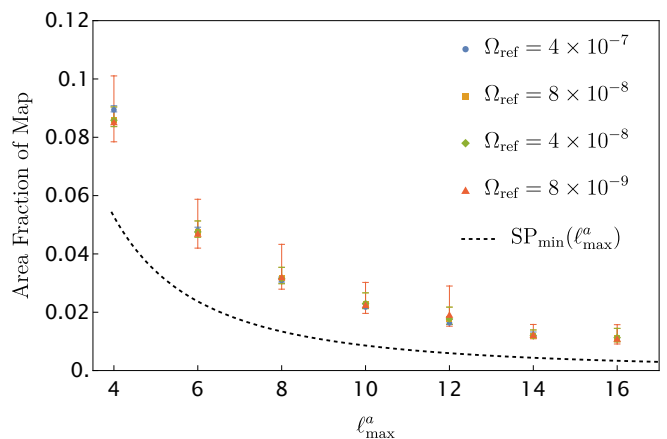


FIG. 2. Spot size given by FWHM vs. ℓ_{max}^a for various choices of Ω_{ref} during $T_{\text{obs}} = 3$ months. Error bars mark 95% confidence intervals. The dashed line shows the approximate minimum value of the SP metric for a spherical harmonic description with a given ℓ_{max}^a ; see Eq. (7) and surrounding discussion.

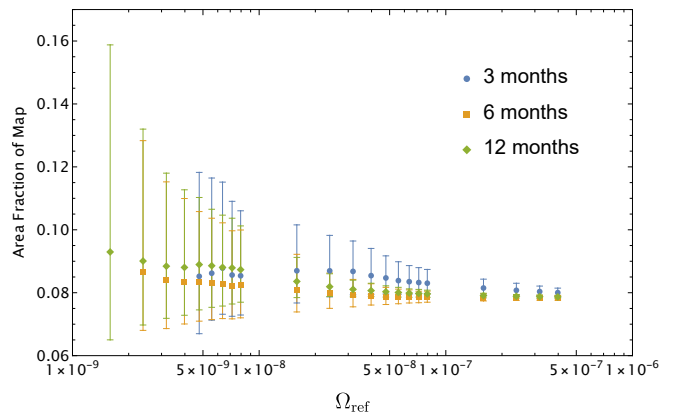


FIG. 3. Spot size given by FWHM vs. Ω_{ref} for various choices of T_{obs} with $\ell_{\text{max}}^a = 4$.

we find that the recovery of a single point source signal has a binary dependence on the overall ASGWB signal amplitude for a given observing duration (equivalently, the signal-to-noise ratio of the ASGWB). If $\Omega_{\text{ref}} \gtrsim 10^{-8}$ for 1 year of data, the spatial distribution of the signal is recovered for $\ell_{\text{max}}^a = 4$, but increasing Ω_{ref} beyond that point does not improve angular resolution as measured by the SP metric (although it does reduce the parameter uncertainty and therefore the overall skymap/SP metric uncertainty). This behavior effectively defines a noise floor for each spherical harmonic mode. It will be important to characterize this noise floor; however, doing so will require meaningful consideration of low-amplitude ASGWBs and thus inclusion of the anisotropic Galactic foreground. As such, further exploration of this point is beyond the scope of this study and should be pursued in future work.

B. Two Point Source

For the two-point case, the orbital motion of the LISA constellation becomes highly relevant until completing at least half an orbit; for three months of data, the two point sources were largely unresolvable for all considered amplitudes of the simulated signal. We therefore report results for $T_{\text{obs}} = 6$ months.

1. Dependence on ℓ_{max}^a

Consistent with the results in §III A, the choice of a higher ℓ_{max}^a increases LISA's ability to resolve two ASGWB sources as measured by the TP metric, with the exception of $\ell_{\text{max}}^a = 8$ at $\Delta\phi = \pi$. Note that the data point for $\ell_{\text{max}}^a = 10$ at $\Delta\phi = 4\pi/5$ is marked with a †; analysis of the original simulation recovered a significant bimodality in the two-point metric. This resulted in disproportionately large error in our measurement of the two-point metric at this ℓ_{max}^a and separation. Repeating the simulation with identical parameters, save that the injected points sources are translated on the sky (see Table III), results in a non-bimodal recovery with uncertainty that is consistent with the overall trend. This indicates that the original bimodality was likely a result of interaction with the directional LISA response due to the specific locations of the point sources on the sky and the relatively short T_{obs} used in this simulation. We therefore use the measurement of the two-point metric obtained from the second, translated simulation for the data point marked with the † in Fig. 5.

2. Dependence on ASGWB Amplitude

We additionally consider different values of the simulated ASGWB amplitude Ω_{ref} for $\ell_{\text{max}}^a = 8$ in Fig. 6. The drop in the TP metric from $\Delta\phi = 2\pi/5$ to $\Delta\phi = 3\pi/5$ present in Fig. 5 is no longer present with higher Ω_{ref} , and the low TP metric of the $\ell_{\text{max}}^a = 8$ case from above is greatly improved. In conjunction with the single-point results, this behavior again implies a statistical noise floor that depends both on the SNR of the ASGWB and the number of parameters used to model it; recall that for a given $\ell_{\text{max}}^a = 2\ell_{\text{max}}^b$, the spherical harmonic spatial model has $\sum_{\ell=1}^{\ell_{\text{max}}^b} (2\ell + 1)$ free parameters.

The recovered TP metric is compared to the TP heuristic in Fig. 2. The observed trend is somewhat shallower in slope, but similarly linear (modulo some scatter at lower amplitudes). The difference in slope is likely in part explained by the offset of the SP metric heuristic from the data as seen in Fig. 2.

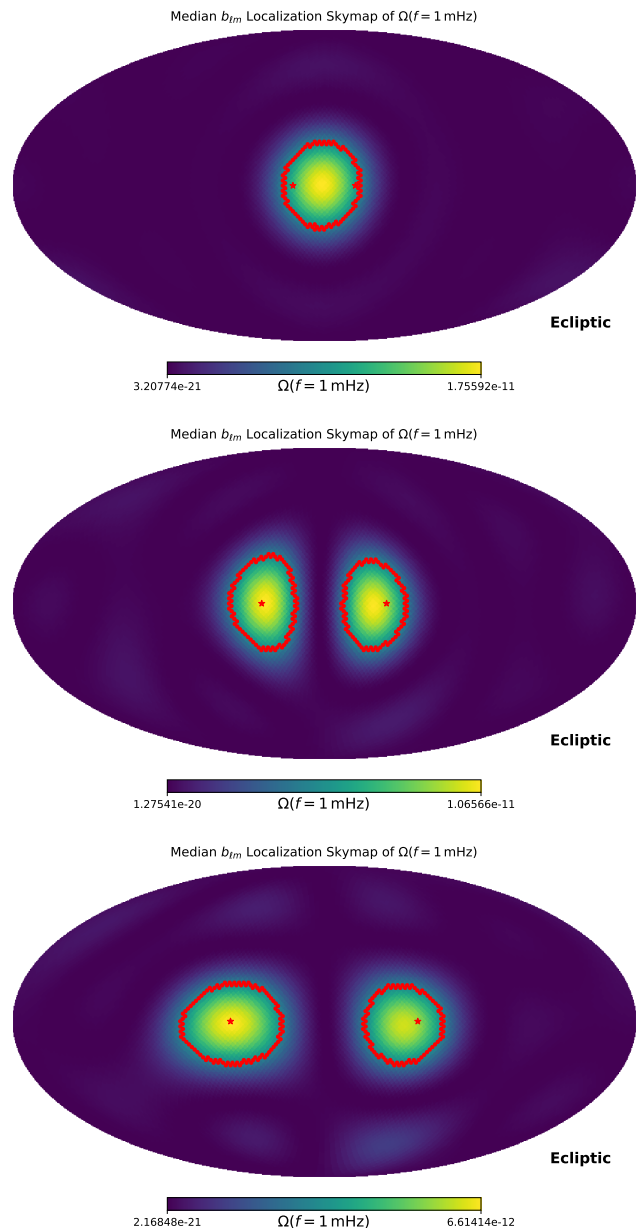


FIG. 4. Posterior median ASGWB energy density skymaps with FWHM contours shown in red and the true (simulated) locations of the point sources indicated with a red star. These plots were produced via the analyses discussed in §II B-II C for simulated ASGWBs with $\Omega_{\text{ref}} = 8 \times 10^{-9}$, $\ell_{\text{max}}^a = 8$, $T_{\text{obs}} = 6$ months, and (from top to bottom) $\Delta\phi = \pi/5$, $2\pi/5$, $3\pi/5$. As $\Delta\phi$ decreases, the ability to resolve two point sources diminishes.

IV. DISCUSSION AND CONCLUSIONS

We investigate the angular resolution of a Bayesian spherical harmonic search for ASGWBs in LISA. We use BLIP to simulate and analyze single-point and two-point source ASGWBs across a broad parameter space for both signal simulation and recovery. These include ASGWB

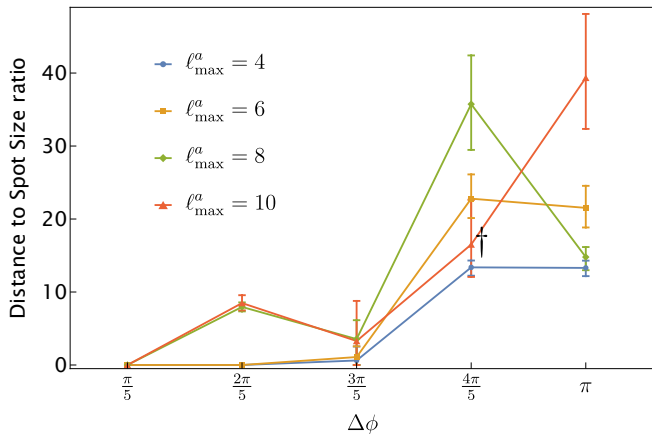


FIG. 5. Distance to spot size ratio (TP metric) vs. injected angular separation for various choices of ℓ_{\max}^a during a 6 month observation. The point marked with † is simulated with different sky locations (see Table III).

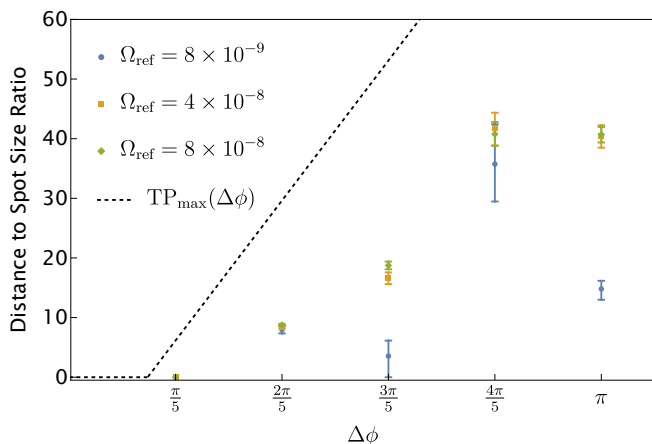


FIG. 6. Distance to spot size ratio (TP metric) vs. injected angular separation for various choices of Ω_{ref} for $\ell_{\max}^a = 8$. The dashed line shows the approximate maximum value of the TP metric at $\ell_{\max}^a = 8$ for a given $\Delta\phi$; see Eq. (8) and surrounding discussion.

amplitude, total observing time, choice of spherical harmonic truncation ℓ_{\max}^a , and — for the two-point case — angular separation of the component sources on the angular resolution of our Bayesian spherical harmonic ASGWB analysis. We quantitatively characterize these factors’ associated trends in angular resolution using two metrics, both based off of the FWHM measure.

For middling-to-high-amplitude⁶ ASGWBs ($\Omega_{\text{ref}}(f = 25 \text{ Hz}) > 10^{-9}$ for 1 year of observing time, given the LISA detector noise assumed in this work), we find that

⁶ (i.e., somewhat less than the amplitude of the Galactic foreground, although we only consider the case of a $\alpha = 2/3$ power law; the impact of assumed spectral form on Bayesian ASGWB searches should be considered in future work.)

the choice of ℓ_{\max}^a is the primary determining factor for the search’s angular resolution. This remains true up to the highest ℓ_{\max}^a considered in this work, $\ell_{\max}^a = 16$. Higher choices of ℓ_{\max}^a would presumably continue this trend (although not indefinitely), but are not currently feasible due to the intensive computational cost of modelling the LISA detector response to each additional spherical harmonic mode and the difficulty of efficiently sampling such a high-dimensional parameter space.

The ASGWB amplitude, parameterized by the dimensionless energy density Ω_{ref} , has no discernible impact on the angular resolution of the search as long as the overall SNR for a given observing duration is sufficiently high to recover a signal. That being said, larger amplitudes/longer observing durations do improve the uncertainty of the recovery, as would be expected. It is worth noting that particularly short observing durations have severe negative impacts on the ASGWB recovery quality. As this effect is due to the fact that short observing times do not gain the full advantage of the LISA constellation’s orbital motion, the negative impacts are mitigated by $T_{\text{obs}} \geq 6$ months and can therefore be expected to be negligible when considering the full LISA mission duration. However, early iterations of global fit analyses during the first 3 – 6 months of the LISA mission could be impacted.

At low SNR, however, we observe a threshold below which the combination of instrumental and statistical noise render the search entirely unable to characterize the ASGWB spatial distribution with a given ℓ_{\max}^a . It is reasonable to infer that for low-SNR ASGWBs, the angular resolution of the search will be information-limited. That is, for a Bayesian search where the angular resolution is primarily determined by the choice of ℓ_{\max}^a — and accordingly, the number of parameters in the ASGWB spatial model — the amount of information contained in the signal will limit how many such parameters can be constrained, therefore limiting the angular resolution. A detailed study of this SNR threshold and its dependence on ℓ_{\max}^a is a promising direction for future work.

Furthermore, the behavior in Fig. 5 highlights some imperfections in the method used to discern between multiple overlapping ASGWBs. As the TP metric contours are computed at one half of the local maximum energy density, this method will not always be able to distinguish between two peaks even if they are present in the posterior results. One could instead try computing 90% of the peak energy density, but this confronts separate concerns such as whether that metric fully characterizes the point-spread of the source, or more technical difficulties relating to the discreteness of the choice in \mathbf{n}_{side} . While the methods used in this work suffice for the spatial scales that are currently computationally accessible, more robust methods should be developed to distinguish between multiple ASGWB contributors at the finer scales that computational advances will grant access to. Such methods would then allow for ASGWB separation through (for instance) targeted directional searches with independent

spectral models.

Our primary conclusion is that, while the limitations of LISA’s angular response are expected to become relevant eventually, the angular resolution achievable by Bayesian spherical harmonic ASGWB searches in LISA is currently limited at high amplitudes by the choice of ℓ_{\max}^a , and therefore driven by current computational limitations. As continued development of software like BLIP and computational advancements will reduce the cost of higher ℓ_{\max}^a analyses, we expect the eventual angular resolution of Bayesian searches for high-amplitude ASGWBs in LISA to be better than what we report here. Notably, this result exceeds the angular sensitivity expected for frequentist approaches to characterizing the LISA angular power spectrum [e.g., 16, 42–44] for the frequency range considered. The upper limit achieved in this work of $\ell_{\max}^a = 16$ exceeds even the $\ell_{\max}^a \lesssim 15$ of Contaldi *et al.* [44] for the equivalent case of a high-SNR ASGWB in well-understood noise. It is additionally worth noting that when we reconstitute the $a_{\ell m s}$ from the $b_{\ell m s}$, we observe an insensitivity to odd ℓ_a modes, consistent with the calculations presented in e.g., Bartolo *et al.* [19], Kudoh and Taruya [42]; see Fig. 7 and discussion in Appendix A.

Finally, it is important to note that we do not consider additional complicating factors such as breathing modes of the LISA constellation or sources of nonstationary noise in the LISA detector, both of which will affect LISA’s overall sensitivity to SGWBs [54, 55]. Nor do we consider a realistic treatment of searches for underlying ASGWBs in the presence of the Galactic foreground. The impact of these factors on the efficacy and angular resolution of Bayesian LISA ASGWB searches should be investigated in future work. As such, this work does not extend to investigation of realistic astrophysical

ASGWBs in LISA. While the BLIP anisotropic analysis has been applied to local ASGWBs such as that of the Galaxy [38] and the Large Magellanic Cloud [6], a crucial direction of future exploration will be the extragalactic SGWB from stellar-origin black hole binaries [e.g., 8]. This SGWB will possess a kinematic dipole and small intrinsic anisotropies on the level of the large-scale structure of the Universe; these latter anisotropies may even hold the key to spectral separation between this astrophysical SGWB and an underlying signal of cosmological origin. It will therefore be important in the future to explore LISA’s ability (or lack thereof) to characterize the anisotropies of low-amplitude, extragalactic ASGWBs in the presence of the Galactic foreground over its full nominal (4 year) and extended (10 year) mission durations.

ACKNOWLEDGEMENTS

The authors would like to thank Erik Floden, Sharan Banagiri, Steven Rieck, Jessica Lawrence, and Joseph Romano for many helpful conversations. This work is supported by the NASA grant 90NSSC19K0318, and utilized computing resources provided by the Minnesota Supercomputing Institute at the University of Minnesota.

DATA AVAILABILITY

BLIP is open source and is available at <https://github.com/sharanbng/blip>. Simulation parameters and posterior samples for all analyses are available on Zenodo [56].

-
- [1] P. Amaro-Seoane, H. Audley, S. Babak, *et al.*, *Laser Interferometer Space Antenna* (2017).
 - [2] P. Amaro-Seoane, J. Andrews, M. Arca Sedda, *et al.*, *Living Reviews in Relativity* **26**, 2 (2023).
 - [3] G. Agazie, A. Anumalapudi, A. M. Archibald, *et al.*, *The Astrophysical Journal Letters* **951**, L8 (2023).
 - [4] J. A. Edlund, M. Tinto, A. Krolak, and G. Nelemans, *Physical Review D* **71**, 122003 (2005), [arxiv:gr-qc/0504112](https://arxiv.org/abs/astro-ph/0504112).
 - [5] A. J. Rüter, K. Belczynski, M. Benacquista, *et al.*, *The Astrophysical Journal* **717**, 1006 (2010), [arxiv:0705.3272](https://arxiv.org/abs/0705.3272).
 - [6] S. Rieck, A. W. Criswell, V. Korol, *et al.*, *A Stochastic Gravitational Wave Background in LISA from Unresolved White Dwarf Binaries in the Large Magellanic Cloud* (2024), [arxiv:2308.12437](https://arxiv.org/abs/2308.12437) [astro-ph, physics:gr-qc].
 - [7] F. Pozzoli, S. Babak, A. Sesana, *et al.*, *Computation of stochastic background from extreme mass ratio inspiral populations for LISA* (2023), [arxiv:2302.07043](https://arxiv.org/abs/2302.07043) [astro-ph].
 - [8] S. Babak, C. Caprini, D. G. Figueroa, *et al.*, *Stochastic gravitational wave background from stellar origin binary black holes in LISA* (2023), [arxiv:2304.06368](https://arxiv.org/abs/2304.06368) [astro-ph, physics:gr-qc].
 - [9] C. Caprini and D. G. Figueroa, *Classical and Quantum Gravity* **35**, 163001 (2018).
 - [10] L. Bethke, D. G. Figueroa, and A. Rajantie, *Physical Review Letters* **111**, 011301 (2013).
 - [11] M. Geller, A. Hook, R. Sundrum, and Y. Tsai, *Physical Review Letters* **121**, 201303 (2018).
 - [12] N. Bartolo, D. Bertacca, V. D. Luca, *et al.*, *Journal of Cosmology and Astroparticle Physics* **2020** (02), 028.
 - [13] C. R. Contaldi, *Physics Letters B* **771**, 9 (2017).
 - [14] N. Bartolo, D. Bertacca, S. Matarrese, *et al.*, *Physical Review D* **100**, 121501 (2019).
 - [15] N. Bartolo, D. Bertacca, S. Matarrese, *et al.*, *Physical Review D* **102**, 023527 (2020), [arxiv:1912.09433](https://arxiv.org/abs/1912.09433) [astro-ph].
 - [16] K. Breivik, C. M. F. Mingarelli, and S. L. Larson, *The Astrophysical Journal* **901**, 4 (2020).
 - [17] G. Cusin, C. Pitrou, and J.-P. Uzan, *Physical Review D* **97**, 123527 (2018), [arxiv:1711.11345](https://arxiv.org/abs/1711.11345) [astro-ph, physics:gr-qc, physics:hep-th].

- [18] G. Cusin, I. Dvorkin, C. Pitrou, and J.-P. Uzan, *Physical Review Letters* **120**, 231101 (2018), arxiv:1803.03236 [astro-ph, physics:gr-qc, physics:hep-th].
- [19] N. Bartolo, D. Bertacca, R. Caldwell, *et al.*, *Journal of Cosmology and Astroparticle Physics* **2022** (11), 009, arxiv:2201.08782 [astro-ph, physics:gr-qc].
- [20] E. Floden, V. Mandic, A. Matas, and L. Tsukada, *Physical Review D* **106**, 023010 (2022), arxiv:2203.17141 [astro-ph, physics:gr-qc].
- [21] R. Abbott, T. D. Abbott, S. Abraham, *et al.*, *Physical Review D* **104**, 022005 (2021).
- [22] Y. Ali-Haïmoud, T. L. Smith, and C. M. F. Mingarelli, *Physical Review D* **102**, 122005 (2020), arxiv:2006.14570 [astro-ph, physics:gr-qc, physics:physics].
- [23] C. M. F. Mingarelli, T. Sidery, I. Mandel, and A. Vecchio, *Physical Review D* **88**, 062005 (2013).
- [24] S. R. Taylor and J. R. Gair, *Physical Review D* **88**, 084001 (2013).
- [25] S. R. Taylor, R. van Haasteren, and A. Sesana, *Physical Review D* **102**, 084039 (2020).
- [26] N. J. Cornish and R. van Haasteren, *Mapping the nano-Hertz gravitational wave sky* (2014), arxiv:1406.4511 [astro-ph, physics:gr-qc].
- [27] G. Agazie, A. Anumarlapudi, A. M. Archibald, *et al.*, *The NANOGrav 15-year Data Set: Search for Anisotropy in the Gravitational-Wave Background* (2023), arxiv:2306.16221 [astro-ph, physics:gr-qc].
- [28] N. J. Cornish, *Class. Quant. Grav.* **18**, 4277 (2001), arXiv:astro-ph/0105374.
- [29] C. Ungarelli and A. Vecchio, *Phys. Rev. D* **64**, 121501 (2001), arXiv:astro-ph/0106538.
- [30] H. Kudoh and A. Taruya, *Phys. Rev. D* **71**, 024025 (2005), arXiv:gr-qc/0411017.
- [31] A. Taruya and H. Kudoh, *Phys. Rev. D* **72**, 104015 (2005), arXiv:gr-qc/0507114.
- [32] A. Taruya, *Phys. Rev. D* **74**, 104022 (2006), arXiv:gr-qc/0607080.
- [33] A. Renzini and C. Contaldi, *Mon. Not. Roy. Astron. Soc.* **481**, 4650 (2018), arXiv:1806.11360 [astro-ph.IM].
- [34] R. Buscicchio, A. Klein, V. Korol, *et al.*, *A test for LISA foreground Gaussianity and stationarity. I. Galactic white-dwarf binaries* (2024), arXiv:2410.08263 [astro-ph].
- [35] M. Piarulli, R. Buscicchio, F. Pozzoli, *et al.*, *A test for LISA foreground Gaussianity and stationarity. II. Extreme mass-ratio inspirals* (2024), arXiv:2410.08862 [astro-ph].
- [36] F. Pozzoli, R. Buscicchio, A. Klein, *et al.*, *Cyclostationary signals in LISA: A practical application to Milky Way satellites* (2024), arXiv:2410.08274.
- [37] A. W. Criswell, S. Rieck, and V. Mandic, *Templated Anisotropic Analyses of the LISA Galactic Foreground* (2024), arXiv:2410.23260 [astro-ph].
- [38] S. Banagiri, A. Criswell, T. Kuan, *et al.*, *Monthly Notices of the Royal Astronomical Society* **507**, 5451 (2021).
- [39] M. Peterseim, O. Jennrich, K. Danzmann, and B. F. Schutz, *Classical and Quantum Gravity* **14**, 1507 (1997).
- [40] C. Cutler, *Physical Review D* **57**, 7089 (1998).
- [41] T. A. Moore and R. W. Hellings, *Physical Review D* **65**, 062001 (2002).
- [42] H. Kudoh and A. Taruya, *Physical Review D* **71**, 024025 (2005).
- [43] A. Taruya and H. Kudoh, *Physical Review D* **72**, 104015 (2005).
- [44] C. R. Contaldi, M. Pieroni, A. I. Renzini, *et al.*, *Physical Review D* **102**, 043502 (2020), arxiv:2006.03313 [astro-ph].
- [45] G. Mentasti, C. R. Contaldi, and M. Peloso, *Probing the galactic and extragalactic gravitational wave backgrounds with space-based interferometers* (2024), arXiv:2312.10792 [astro-ph, physics:gr-qc].
- [46] T. B. Littenberg and N. J. Cornish, *Prototype Global Analysis of LISA Data with Multiple Source Types* (2023), arxiv:2301.03673 [astro-ph, physics:gr-qc].
- [47] M. L. Katz, N. Karnesis, N. Korsakova, *et al.*, *An efficient GPU-accelerated multi-source global fit pipeline for LISA data analysis* (2024), arXiv:2405.04690 [astro-ph, physics:gr-qc].
- [48] N. J. Cornish and S. L. Larson, *Classical and Quantum Gravity* **18**, 3473 (2001), arxiv:gr-qc/0103075.
- [49] N. J. Cornish, *Physical Review D* **65**, 022004 (2001).
- [50] J. S. Speagle, *Monthly Notices of the Royal Astronomical Society* **493**, 3132 (2020).
- [51] K. M. Gorski, E. Hivon, A. J. Banday, *et al.*, *The Astrophysical Journal* **622**, 759 (2005), arXiv:astro-ph/0409513.
- [52] M. Tinto and S. V. Dhurandhar, *Living Reviews in Relativity* **24**, 1 (2020).
- [53] M. R. Adams and N. J. Cornish, *Physical Review D* **82**, 022002 (2010), arxiv:1002.1291.
- [54] O. Hartwig, M. Lilley, M. Muratore, and M. Pieroni, *Physical Review D* **107**, 123531 (2023).
- [55] M. Muratore, J. Gair, and L. Speri, *Impact of the noise knowledge uncertainty for the science exploitation of cosmological and astrophysical stochastic gravitational wave background with LISA* (2023), arxiv:2308.01056 [astro-ph, physics:gr-qc].
- [56] M. Bloom, A. Criswell, and V. Mandic, *Datasets for "Angular Resolution of a Bayesian Search for Anisotropic Stochastic Gravitational Wave Backgrounds with LISA"* (2024).

Appendix A: Insensitivity to Odd- ℓ_a Modes

We consider in brief the insensitivity of LISA to odd- ℓ_a spherical harmonic modes discussed in [19, 42]. Transforming our $b_{\ell m}$ posterior samples back to the $a_{\ell m}$ basis, we find that the odd $a_{\ell m}$ s are recovered to be consistent with zero (whereas the even modes are, generally, not). Fig. 7 shows the transformed $a_{\ell m}$ posterior distribution for two-point simulation no. 116 (analyzed with $\ell_{\max}^a = 8$; see Table III), including only $m = 0$ terms for legibility.

Appendix B: Simulation Details

Table II (III) includes the values of all simulation/analysis settings for the single-point (two-point) simulations discussed in this work. These parameters are described in §II B.

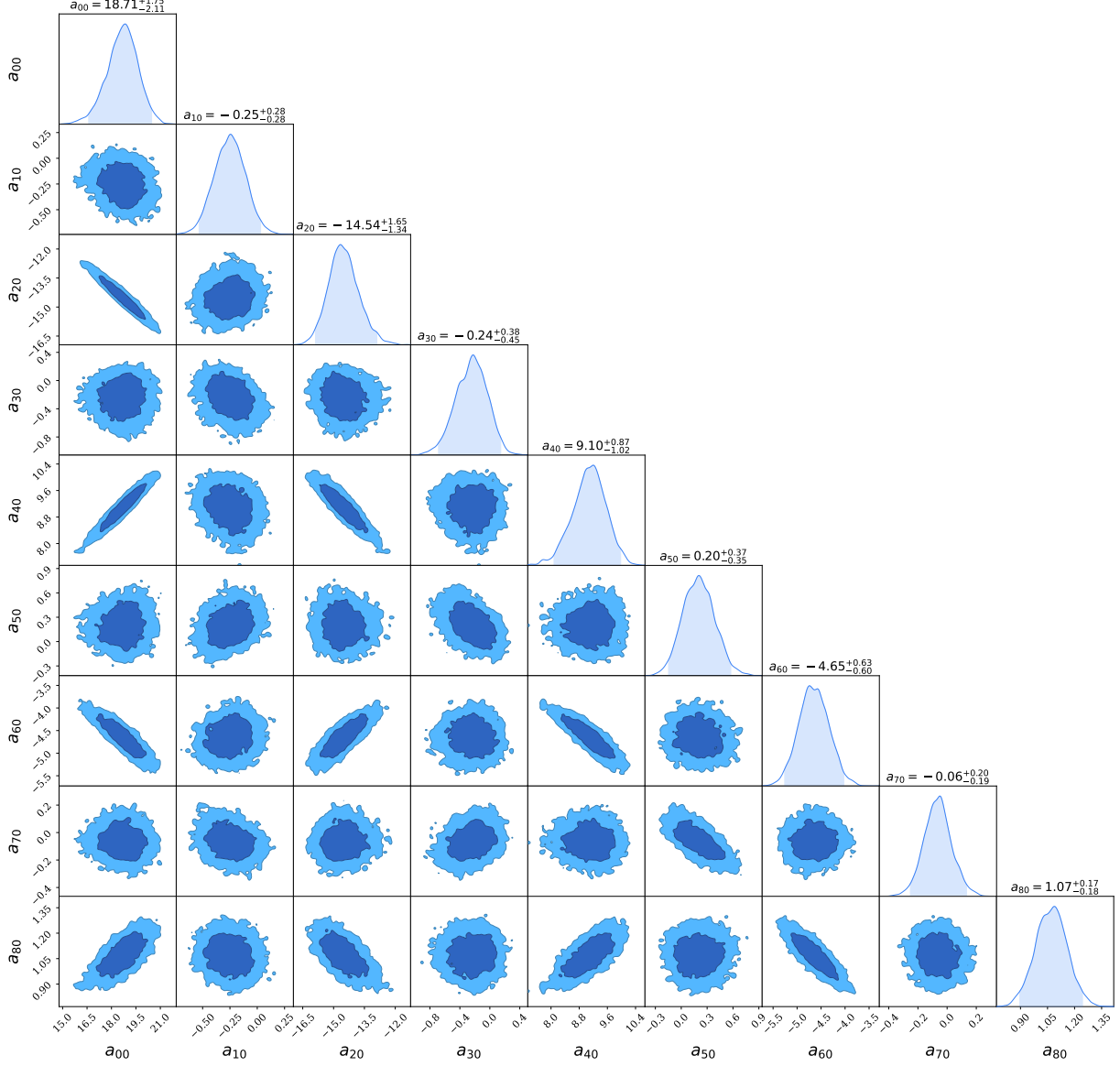


FIG. 7. Transformed $a_{\ell m}$ posterior samples for simulation 116 ($\ell_{\max}^a = 8$). Only $m = 0$ terms are shown so as to preserve the legibility of the corner plot. Quoted bounds are the mean and 95% C.I. of the posterior samples. The shading in the one-dimensional posterior distribution denotes the 95% C.I.; the dark and light shaded regions of the two-dimensional distributions denote 1- and 2σ bounds, respectively. Note that while the even- ℓ_a modes are well-recovered, the odd- ℓ_a mode posterior distributions are all consistent with zero.

TABLE II: Single-point simulations.

Simulation	ℓ_{\max}^a	Ω_{ref}	T_{obs} (months)	$\ell_{\max, \text{inj}}^a$	θ	ϕ
1	4	8.0×10^{-9}	3	16	$\pi/2$	$\pi/2$
2	6	8.0×10^{-9}	3	16	$\pi/2$	$\pi/2$
3	8	8.0×10^{-9}	3	16	$\pi/2$	$\pi/2$
4	10	8.0×10^{-9}	3	16	$\pi/2$	$\pi/2$
5	12	8.0×10^{-9}	3	16	$\pi/2$	$\pi/2$
6	14	8.0×10^{-9}	3	16	$\pi/2$	$\pi/2$
7	16	8.0×10^{-9}	3	16	$\pi/2$	$\pi/2$
8	4	4.0×10^{-8}	3	16	$\pi/2$	$\pi/2$
9	6	4.0×10^{-8}	3	16	$\pi/2$	$\pi/2$
10	8	4.0×10^{-8}	3	16	$\pi/2$	$\pi/2$
11	10	4.0×10^{-8}	3	16	$\pi/2$	$\pi/2$
12	12	4.0×10^{-8}	3	16	$\pi/2$	$\pi/2$
13	14	4.0×10^{-8}	3	16	$\pi/2$	$\pi/2$
14	16	4.0×10^{-8}	3	16	$\pi/2$	$\pi/2$
15	4	8.0×10^{-8}	3	16	$\pi/2$	$\pi/2$
16	6	8.0×10^{-8}	3	16	$\pi/2$	$\pi/2$
17	8	8.0×10^{-8}	3	16	$\pi/2$	$\pi/2$
18	10	8.0×10^{-8}	3	16	$\pi/2$	$\pi/2$
19	12	8.0×10^{-8}	3	16	$\pi/2$	$\pi/2$
20	14	8.0×10^{-8}	3	16	$\pi/2$	$\pi/2$
21	16	8.0×10^{-8}	3	16	$\pi/2$	$\pi/2$
22	4	4.0×10^{-7}	3	16	$\pi/2$	$\pi/2$
23	6	4.0×10^{-7}	3	16	$\pi/2$	$\pi/2$
24	8	4.0×10^{-7}	3	16	$\pi/2$	$\pi/2$
25	10	4.0×10^{-7}	3	16	$\pi/2$	$\pi/2$
26	12	4.0×10^{-7}	3	16	$\pi/2$	$\pi/2$
27	14	4.0×10^{-7}	3	16	$\pi/2$	$\pi/2$
28	16	4.0×10^{-7}	3	16	$\pi/2$	$\pi/2$
29	4	4.8×10^{-9}	3	4	$\pi/2$	$\pi/2$
30	4	5.6×10^{-9}	3	4	$\pi/2$	$\pi/2$
31	4	6.4×10^{-9}	3	4	$\pi/2$	$\pi/2$
32	4	7.2×10^{-9}	3	4	$\pi/2$	$\pi/2$
33	4	8.0×10^{-9}	3	4	$\pi/2$	$\pi/2$
34	4	1.6×10^{-8}	3	4	$\pi/2$	$\pi/2$
35	4	2.4×10^{-8}	3	4	$\pi/2$	$\pi/2$
36	4	3.2×10^{-8}	3	4	$\pi/2$	$\pi/2$
37	4	4.0×10^{-8}	3	4	$\pi/2$	$\pi/2$
38	4	4.8×10^{-8}	3	4	$\pi/2$	$\pi/2$
39	4	5.6×10^{-8}	3	4	$\pi/2$	$\pi/2$
40	4	6.4×10^{-8}	3	4	$\pi/2$	$\pi/2$
41	4	7.2×10^{-8}	3	4	$\pi/2$	$\pi/2$
42	4	8.0×10^{-8}	3	4	$\pi/2$	$\pi/2$
43	4	1.6×10^{-7}	3	4	$\pi/2$	$\pi/2$
44	4	2.4×10^{-7}	3	4	$\pi/2$	$\pi/2$
45	4	3.2×10^{-7}	3	4	$\pi/2$	$\pi/2$
46	4	4.0×10^{-7}	3	4	$\pi/2$	$\pi/2$
47	4	2.4×10^{-9}	6	4	$\pi/2$	$\pi/2$
48	4	3.2×10^{-9}	6	4	$\pi/2$	$\pi/2$
49	4	4.0×10^{-9}	6	4	$\pi/2$	$\pi/2$
50	4	4.8×10^{-9}	6	4	$\pi/2$	$\pi/2$

Continued on next page

TABLE II – continued from previous page

Simulation	ℓ_{\max}^a	Ω_{ref}	T_{obs}	$\ell_{\max, \text{inj}}^a$	θ	ϕ
51	4	5.6×10^{-9}	6	4	$\pi/2$	$\pi/2$
52	4	6.4×10^{-9}	6	4	$\pi/2$	$\pi/2$
53	4	7.2×10^{-9}	6	4	$\pi/2$	$\pi/2$
54	4	8.0×10^{-9}	6	4	$\pi/2$	$\pi/2$
55	4	1.6×10^{-8}	6	4	$\pi/2$	$\pi/2$
56	4	2.4×10^{-8}	6	4	$\pi/2$	$\pi/2$
57	4	3.2×10^{-8}	6	4	$\pi/2$	$\pi/2$
58	4	4.0×10^{-8}	6	4	$\pi/2$	$\pi/2$
59	4	4.8×10^{-8}	6	4	$\pi/2$	$\pi/2$
60	4	5.6×10^{-8}	6	4	$\pi/2$	$\pi/2$
61	4	6.4×10^{-8}	6	4	$\pi/2$	$\pi/2$
62	4	7.2×10^{-8}	6	4	$\pi/2$	$\pi/2$
63	4	8.0×10^{-8}	6	4	$\pi/2$	$\pi/2$
64	4	1.6×10^{-7}	6	4	$\pi/2$	$\pi/2$
65	4	2.4×10^{-7}	6	4	$\pi/2$	$\pi/2$
66	4	3.2×10^{-7}	6	4	$\pi/2$	$\pi/2$
67	4	4.0×10^{-8}	6	4	$\pi/2$	$\pi/2$
68	4	1.6×10^{-9}	12	4	$\pi/2$	$\pi/2$
69	4	2.4×10^{-9}	12	4	$\pi/2$	$\pi/2$
70	4	3.2×10^{-9}	12	4	$\pi/2$	$\pi/2$
71	4	4.0×10^{-9}	12	4	$\pi/2$	$\pi/2$
72	4	4.8×10^{-9}	12	4	$\pi/2$	$\pi/2$
73	4	5.6×10^{-9}	12	4	$\pi/2$	$\pi/2$
74	4	6.4×10^{-9}	12	4	$\pi/2$	$\pi/2$
75	4	7.2×10^{-9}	12	4	$\pi/2$	$\pi/2$
76	4	8.0×10^{-9}	12	4	$\pi/2$	$\pi/2$
77	4	1.6×10^{-8}	12	4	$\pi/2$	$\pi/2$
78	4	2.4×10^{-8}	12	4	$\pi/2$	$\pi/2$
79	4	3.2×10^{-8}	12	4	$\pi/2$	$\pi/2$
80	4	4.0×10^{-8}	12	4	$\pi/2$	$\pi/2$
81	4	4.8×10^{-8}	12	4	$\pi/2$	$\pi/2$
82	4	5.6×10^{-8}	12	4	$\pi/2$	$\pi/2$
83	4	6.4×10^{-8}	12	4	$\pi/2$	$\pi/2$
84	4	7.2×10^{-8}	12	4	$\pi/2$	$\pi/2$
85	4	8.0×10^{-8}	12	4	$\pi/2$	$\pi/2$
86	4	1.6×10^{-7}	12	4	$\pi/2$	$\pi/2$
87	4	2.4×10^{-7}	12	4	$\pi/2$	$\pi/2$
88	4	3.2×10^{-7}	12	4	$\pi/2$	$\pi/2$
89	4	4.0×10^{-7}	12	4	$\pi/2$	$\pi/2$

TABLE II: List of single point source simulations used in this paper. Simulations 1-28 are reported in Fig. 2. Simulations 29-89 are reported in Fig. 3.

TABLE III: Two-point simulations.

Simulation	ℓ_{\max}^a	Ω_{ref}	T_{obs} (months)	$\ell_{\max, \text{inj}}^a$	θ_1	ϕ_1	θ_2	ϕ_2	$\Delta\phi$
90	4	8.0×10^{-9}	6	12	$\pi/2$	$\pi/5$	$\pi/2$	$-\pi/5$	$2\pi/5$
91	6	8.0×10^{-9}	6	12	$\pi/2$	$\pi/5$	$\pi/2$	$-\pi/5$	$2\pi/5$
92	8	8.0×10^{-9}	6	12	$\pi/2$	$\pi/5$	$\pi/2$	$-\pi/5$	$2\pi/5$
93	10	8.0×10^{-9}	6	12	$\pi/2$	$\pi/5$	$\pi/2$	$-\pi/5$	$2\pi/5$
94	4	8.0×10^{-9}	6	12	$\pi/2$	$2\pi/5$	$\pi/2$	$-2\pi/5$	$4\pi/5$
95	6	8.0×10^{-9}	6	12	$\pi/2$	$2\pi/5$	$\pi/2$	$-2\pi/5$	$4\pi/5$
96	8	8.0×10^{-9}	6	12	$\pi/2$	$2\pi/5$	$\pi/2$	$-2\pi/5$	$4\pi/5$
97	10	8.0×10^{-9}	6	12	$\pi/2$	$2\pi/5$	$\pi/2$	$-2\pi/5$	$4\pi/5$
98 [†]	10	8.0×10^{-9}	6	12	$\pi/2$	0	$\pi/2$	$-4\pi/5$	$4\pi/5$
99	4	8.0×10^{-9}	6	12	$\pi/2$	$3\pi/5$	$\pi/2$	$-3\pi/5$	$6\pi/5$
100	6	8.0×10^{-9}	6	12	$\pi/2$	$3\pi/5$	$\pi/2$	$-3\pi/5$	$6\pi/5$
101	8	8.0×10^{-9}	6	12	$\pi/2$	$3\pi/5$	$\pi/2$	$-3\pi/5$	$6\pi/5$
102	10	8.0×10^{-9}	6	12	$\pi/2$	$3\pi/5$	$\pi/2$	$-3\pi/5$	$6\pi/5$
103	4	8.0×10^{-9}	6	12	$\pi/2$	$4\pi/5$	$\pi/2$	$-4\pi/5$	$8\pi/5$
104	6	8.0×10^{-9}	6	12	$\pi/2$	$4\pi/5$	$\pi/2$	$-4\pi/5$	$8\pi/5$
105	8	8.0×10^{-9}	6	12	$\pi/2$	$4\pi/5$	$\pi/2$	$-4\pi/5$	$8\pi/5$
106	10	8.0×10^{-9}	6	12	$\pi/2$	$4\pi/5$	$\pi/2$	$-4\pi/5$	$8\pi/5$
107	4	8.0×10^{-9}	6	12	$\pi/2$	$\pi/2$	$\pi/2$	$-\pi/2$	π
108	6	8.0×10^{-9}	6	12	$\pi/2$	$\pi/2$	$\pi/2$	$-\pi/2$	π
109	8	8.0×10^{-9}	6	12	$\pi/2$	$\pi/2$	$\pi/2$	$-\pi/2$	π
110	10	8.0×10^{-9}	6	12	$\pi/2$	$\pi/2$	$\pi/2$	$-\pi/2$	π
111	8	4.0×10^{-8}	6	12	$\pi/2$	$\pi/5$	$\pi/2$	$-\pi/5$	$2\pi/5$
112	8	4.0×10^{-8}	6	12	$\pi/2$	$2\pi/5$	$\pi/2$	$-2\pi/5$	$4\pi/5$
113	8	4.0×10^{-8}	6	12	$\pi/2$	$3\pi/5$	$\pi/2$	$-3\pi/5$	$6\pi/5$
114	8	4.0×10^{-8}	6	12	$\pi/2$	$4\pi/5$	$\pi/2$	$-4\pi/5$	$8\pi/5$
115	8	4.0×10^{-8}	6	12	$\pi/2$	$\pi/2$	$\pi/2$	$-\pi/2$	π
116	8	8.0×10^{-8}	6	12	$\pi/2$	$\pi/5$	$\pi/2$	$-\pi/5$	$2\pi/5$
117	8	8.0×10^{-8}	6	12	$\pi/2$	$2\pi/5$	$\pi/2$	$-2\pi/5$	$4\pi/5$
118	8	8.0×10^{-8}	6	12	$\pi/2$	$3\pi/5$	$\pi/2$	$-3\pi/5$	$6\pi/5$
119	8	8.0×10^{-8}	6	12	$\pi/2$	$4\pi/5$	$\pi/2$	$-4\pi/5$	$8\pi/5$
120	8	8.0×10^{-8}	6	12	$\pi/2$	$\pi/2$	$\pi/2$	$-\pi/2$	π

TABLE III: List of two point source simulations used in this paper. Simulations 90-110 are reported in Fig. 5. Simulations 92, 96, 101, 105, 109, and 111-120 are reported in Fig. 6.